Science Advances
AAAS

advances.sciencemag.org/cgi/content/full/7/2/eabc8998/DC1

Supplementary Materials for

Carbon isotope evidence for the global physiology of Proterozoic cyanobacteria

Sarah J. Hurley*, Boswell A. Wing, Claire E. Jasper, Nicholas C. Hill, Jeffrey C. Cameron*

*Corresponding author. Email: sarah.hurley@colorado.edu (S.J.H.); jeffrey.c.cameron@colorado.edu (J.C.C.)

Published 6 January 2021, *Sci. Adv.* **7**, eabc8998 (2021)
DOI: 10.1126/sciadv.abc8998

This PDF file includes:

Supplementary Materials

1. Estimates of O_2, CO_2, and oxygenic productivity through Earth history

In broad brush, the concentration of atmospheric oxygen has increased through Earth history in two steps (Fig. S1). Atmospheric oxygen was negligible in the Archean Eon at $<10^{-6}$ preindustrial atmospheric levels (PAL = 280 ppm CO_2 and 200,000 ppm O_2) (*4*). The Paleoproterozoic accumulation of atmospheric oxygen, the Great Oxidation Event (GOE), was underway by 2.43 Ga, and continued for another ≈200 million years (*60*). Atmospheric oxygen concentrations may have reached near modern levels early in the Paleoproterozoic Era at $\sim10^{-3}$ PAL before returning to values between $\sim10^{-3}$ to $\sim10^{-1}$ PAL in the Mesoproterozoic Era (e.g., *1*, *4*, *8*, *61*). After land plants arose early in the Paleozoic Era, atmospheric oxygen concentrations increased again from 10^{-1} PAL to approximately present levels with some minor variation afterward (*59*). In contrast, atmospheric CO_2 concentrations have decreased, perhaps less dramatically, through time. Archean atmospheric CO_2 concentrations of ~40-400 PAL are consistent with atmospheric and general circulation models (*7*, *8*, *39*). CO_2 levels declined from potentially ~10-100 PAL at the beginning of the Proterozoic Eon to ~1-20 PAL at the end of the Proterozoic (*8*). During the Phanerozoic Eon, modeling predicts a general negative covariation in CO_2 concentrations with O_2 concentrations (*59*).

Environmental, ecological and evolutionary mechanisms have been hypothesized to limit the oxygenic productivity of the marine biosphere on geologic timescales. Some environmental explanations propose nutrient limitation either by phosphorus (*9*, *62*), nitrogen (*10*, *63*), or trace metals (*11*, *64*). Others call on cyanobacterial exclusion from a toxic marine photic zone (*53*, *54*). In ecological scenarios, ecosystem structure is proposed to control oxygen production. Competition between populations of oxygenic and anoxygenic photosynthesizers may have limited oxygenic productivity in the water column

(*12*, *65*). Self-shading within a turbid community of cyanobacteria could have a similar effect on net primary productivity (*66*). Evolutionary hypotheses ascribe limited oxygenic productivity in the Proterozoic to cyanobacteria with enzymatic (*67*), metabolic (*68*), cytological (*69*), or lifestyle (*18*, *55*) traits of their modern descendants. Although ancestral cyanobacteria play a central role in all potential hypotheses for restricting Proterozoic primary productivity, the geologic record contains limited direct evidence for either their global ecological niche or their intracellular physiology at this time.

2. Estimates of Mid-Proterozoic ε_P values by statistical simulation

Statistical simulations provide a way to extract estimated values of ε_P, the isotopic fractionation between dissolved CO_2 and biomass produced via photoautotrophic carbon fixation, from the geologic carbon isotope record. We restricted our analysis to the non-transitional middle Proterozoic interval (1.0-1.8 Ga), identified previously with a mean difference method (*24*), to reduce the confounding effects of non-steady state variation in the carbon isotope record. The entire middle Proterozoic interval was treated as a single time bin as finer time-binning did not affect the results of the statistical analysis (*24*).

We resampled $\delta^{13}C$ values from a previously published, curated dataset (*24*). In this dataset, middle Proterozoic carbonates from a variety of depositional settings, including open and shallow marine environments, have homogeneous $\delta^{13}C$ values with a mean and standard deviation of 0 ± 1.5 ‰ (Fig. S2). This homogeneity likely reflects the geographically uniform nature of the marine bicarbonate reservoir (*70*). Total organic carbon measurements in this dataset similarly reflect a broad range of marine environments and were filtered to exclude demonstrably authigenic and, importantly (*70*), thermally altered sediments (*24*).

Values of ε_{TOC}, the carbon isotopic fractionation between carbonate minerals ($\delta^{13}C_{carb}$) and total organic carbon ($\delta^{13}C_{org}$) preserved in the sedimentary rocks (*24*) is defined as:

(1) $$\varepsilon_{TOC} \equiv \delta^{13}C_{carb} - \delta^{13}C_{org},$$

where $\delta^{13}C_{carb} = [(^{13}C/^{12}C_{carb}/^{13}C/^{12}C_{standard}) - 1] * 1000$ and $\delta^{13}C_{org} = [(^{13}C/^{12}C_{org}/^{13}C/^{12}C_{standard}) - 1] * 1000$, both expressed as permil (‰). Bootstrap resampling of middle Proterozoic carbon isotope records yields an ε_{TOC} distribution with a mean of 28‰ and a range of 20-35‰ (95th percentile; Fig. S2). ε_{TOC} values represent the combined effects of a number of processes including *i*) the fractionation between dissolved CO_2 and the biomass of primary producers (ε_P), *ii*) the fractionation between dissolved CO_2 and carbonate minerals ($\varepsilon_{HCO_3^- - CO_{2\,(aq)}}$, $\varepsilon_{cal/ara-HCO_3^-}$), *iii*) and the fractionation associated with biological reworking of organic carbon during export and burial ($\varepsilon_{reworking}$) (*23*). The isotopic difference between dissolved $CO_{2\,(aq)}$ and biomass produced via photoautotrophic carbon fixation (ε_P) is typically defined by:

(2) $$\varepsilon_P = \delta^{13}C_{CO_{2(aq)}} - \delta^{13}C_{biomass}.$$

We randomly sampled uniform distributions representing fractionation during the conversion and preservation of dissolved CO_2 as carbonate rocks and primary biomass as TOC. The distribution of equilibrium isotope effects between $CO_{2\,(aq)}$ and HCO_3^- ($\varepsilon_{HCO_3^- - CO_{2\,(aq)}}$) ranged from 8.9-11.7‰ (*57*) assuming photic zone temperatures of 3-30°C (e.g., *38*). Experimentally determined kinetic isotope effects associated with the precipitation of calcite and aragonite from HCO_3^- ($\varepsilon_{cal/ara-HCO_3^-}$) ranged from 0.8-3.3‰ (*58*). Fractionations associated with secondary biological processes such as heterotrophic consumption of primary organic matter ($\varepsilon_{reworking}$) ranged from 0-1.5‰ (*23*) (Fig. S2). Values of $\delta^{13}C$ for dissolved $CO_{2\,(aq)}$ and biomass were calculated according to the following approximations:

(3) $$\delta^{13}C_{CO_{2(aq)}} = \delta^{13}C_{carb} - \varepsilon_{cal/ara-HCO_3^-} - \varepsilon_{HCO_3^- - CO_{2\,(aq)}}$$

(4) $$\delta^{13}C_{biomass} = \delta^{13}C_{org} - \varepsilon_{reworking}$$

The resulting distribution of ε_P values, calculated according to Eq. 2, are offset from the ε_{TOC} distribution by ≈12‰, with a mean of 16‰ and a 2σ range of 8-24‰ (Fig. S2). The statistical simulations were run over 10,000 bootstrap trials.

3. Estimates of modern mat ε_P values by statistical simulation

We additionally used these techniques to estimate ε_P values from a published characterization of a modern cyanobacterial mat system (*26*). This mat system was grown and sampled in an experimental pond with a depth of <1 m. The pond was artificially stratified with an anoxic bottom layer of highly concentrated brine and an upper layer diluted with freshwater. We used the same conversion to calculate $\delta^{13}C_{CO_2(aq)}$ values from observed $\delta^{13}C_{carb}$ values, drawing from uniform distributions representing $\varepsilon_{HCO_3^- - CO_{2\,(aq)}}$ at observed pond temperatures of 23-57°C and $\varepsilon_{cal/ara-HCO_3^-}$ (*58*) (Eq. 3; see previous section for full simulation description). We did not include fractionations associated with secondary biological processes ($\varepsilon_{reworking}$) due to the young age of the mat, the anoxic bottom layer, and absence of burial in the system. However, due the small range of $\varepsilon_{reworking}$ (0-1.5‰), the resulting distribution is relatively insensitive to this parameter. Statistical simulations of carbon isotope fractionation in this previously characterized mat system yielded an ε_P distribution with a range of 4-13‰ (95th percentile) and a median value of 8.5‰ (Fig. S3), likely reflecting the impact of limited carbon transport into this hypersaline environment.

4. Culturing Description

Culturing experiments used wild-type (WT) *Synechococcus* sp. strain PCC 7002 (*Synechococcus* 7002) and a Δ*ccm* mutant strain lacking a carboxysome. The Δ*ccm* strain was generated by transforming WT cells in exponential growth phase with 0.5 ng/mL of plasmid DNA, containing a kanamycin resistance cassette flanked by 750 bp homology arms for recombination into the *ccm* locus (*36*). After incubation at 30°C in constant illumination (~150 µmols photons m^{-2} s^{-1}) for 24 hours, transformed cells were selected for with 100 µg/mL kanamycin on A+ media solidified with Bacto Agar (1%; w/v) in 3% (v/v) CO_2. Individual colonies were patched onto new plates and tested for segregation by PCR, using primer pairs specific to either the transformed (primers KAMo0113 and EBJp0048) or WT (primers EBJp0048 and EBJp0006) genome. Presence of the PCR product specific to the transformed genome and absence of the PCR product specific to the WT genome was used as an indicator of full segregation. The 5'-3' sequences for primers are

KAMo0113: CGACTGAATCCGGTGAGAAT,

EBJp0048: CGGTGGAGACGATGATCCG,

and EBJp0006: ATAGGTTCTGAATTGTTCTACTTCTTCGGTGT.

For experiments on carbon isotope fractionation, all cultures grew in A+ media (*71*) at 37°C under saturating light levels of ~227 ± 5 µmol photons m^{-2} s^{-1} provided by cool-white fluorescence lamps.

Cultures were grown in 125 ml conical flasks with foam stoppers (Jaece Industries Identi-plug™), continuously shaking, in an incubator that kept headspace CO_2 constant by continuous replacement with a mixture of CO_2 and air during each experiment. Headspace CO_2 varied across three experimental conditions: 0.04% (v/v) CO_2, 1% (v/v) CO_2, and 3% (v/v) CO_2, corresponding to $CO_{2(aq)}$ concentrations of 7, 180, and 538 µmol kg^{-1}, respectively. The measured pH of the cultures (8.1 in air, 7.3 in 1% CO_2, and 6.7 in 3% CO_2) and the headspace pCO_2 were used to calculate dissolved CO_2 via the csys program (*72*) adapted for the R statistical computing environment. Dissolved CO_2 concentrations calculated for the growth medium ranged from 7 µmol kg^{-1} in air (1× PAL) to 538 µmol kg^{-1} in 3% CO_2 (107 × PAL). We plot both headspace CO_2 levels and dissolved CO_2 concentrations due to the influence of temperature, salinity, and pH on dissolved CO_2 concentrations.

We attempted to grow the Δ*ccm* mutant lacking carboxysomes at both 0.5% (v/v) and 0.8% (v/v) CO_2, corresponding to 18 × PAL and 30 × PAL. However, under our experimental conditions, the mutant strain was only able to grow at 1% CO_2 (36 × PAL) or greater, consistent with the previously observed inability of this high-CO_2-requiring phenotype to grow in air (*31*). Strains were acclimated to each CO_2 condition over the course of four serially-transferred cultures. Cultures grew to an $OD_{730\ nm}$ of ~0.2 before inoculating the next acclimation with 1-3% of the final cell density and harvesting biomass (Fig. S4). Harvested biomass was kept at -70°C. Prior to isotopic analysis, biomass was centrifuged and washed twice with ultrapurified water.

For cultures, values of ε_P were calculated relative to external $\delta^{13}C$ values for $CO_{2(aq)}$ according to:

(5) $$\varepsilon_P = 1000\left[\frac{\left(\delta^{13}C_{CO_{2(aq)}}+1000\right)}{\left(\delta^{13}C_{biomass}+1000\right)} - 1\right]$$

The net specific growth rate of each culture, μ (h^{-1}), was calculated according to:

(6) $$\mu = \frac{\ln(\text{cell density}_{\text{final}}) - \ln(\text{cell density}_{\text{initial}})}{(t_{\text{final}} - t_{\text{initial}})}$$

Initial or final cell densities are in cells ml^{-1} and $t_{\text{final}} - t_{\text{initial}}$ is the duration of each batch culture in hours. Carbon fixation rates (μg C $cell^{-1}$ s^{-1}) were calculated by multiplying the carbon content per cell (μg C $cell^{-1}$) by the net specific growth rate in s^{-1}:

(7) $$C_{\text{fix}} = C_{\text{cell}} \cdot \mu$$

Growth parameters for all cultures are plotted in Fig. S5 and reported in Table S1. Doubling times for the wild-type strain ranged from 5.1 ± 0.7 h grown under air, 3.6 ± 0.6 h grown under 1% CO_2 and 4.0 ± 0.3 h grown under 3% CO_2 on average. Doubling times for the Δ*ccm* mutant grown under equivalent headspaces were slightly greater (slower growth rates) under 1% CO_2 (5.5 ± 1.0 h) and slightly smaller (faster growth rates) under 3% CO_2 (3.5 ± 0.7 h). Carbon fixation rates for the wild-type strain were 67 ± 21, 98 ± 36, and 106 ± 30 fg C $cell^{-1}$ h^{-1} grown under air, 1%, and 3% CO_2, respectively (Table S1). Carbon fixation rates for the Δ*ccm* mutant were 105 ± 33 and 166 ± 44 fg C $cell^{-1}$ h^{-1} grown under 1% and 3% CO_2, respectively. The carbon fixation rates for wild-type strain in air (67± 21 fg C $cell^{-1}$ h^{-1}) are ~3× previously published carbon fixation rates for *Synechococcus* 7002 (*73*).

5. Carbon isotope measurements

The carbon isotope composition of cyanobacterial biomass was measured in the Earth Systems Stable Isotope Lab at the University of Colorado Boulder. Samples were oxidized and combusted with a

Thermo Scientific FlashEA and the resultant CO_2 was analyzed with a Thermo Scientific Delta V Isotope Ratio Mass Spectrometer. Ratios are expressed as $^{13}C/^{12}C$ in units of relative per mil (‰) difference between the sample (R_{sample}) and a standard ($R_{standard}$) of Vienna Peedee Belemnite (VPDB) according to:

(8) $$\delta^{13}C = [(^{13}C/^{12}C_{sample}/^{13}C/^{12}C_{standard}) - 1] * 1000\ (‰)$$

Acetanilide (University of Indiana; $\delta^{13}C$ of -29.53‰; weight % C of 71.09) was used to correct for linearity and drift. Acetanilide was additionally used as a monitoring standard and a bovine gelatin (pugel), from University of California Santa Cruz ($\delta^{13}C$ of -12.62‰; weight % C 44.02) as a discrimination standard.

Isotopic analysis of CO_2 gas was conducted in the Earth Systems Stable Isotope Lab at the University of Colorado Boulder. The CO_2 was analyzed with a Thermo Scientific 253+ Isotope Ratio Mass Spectrometer. The gas was analyzed for four runs with seven cycles at 12.5 volts on 44 m/z with an integration time of 26 s per cycle. Ratios are expressed as $^{13}C/^{12}C$ in units of relative per mil (‰) difference between the sample (R_{sample}) and a standard ($R_{standard}$) of VPBD. The gas was run against an in-house standard that has been corrected against several commercially purchased Oztec bottles of varying compositions.

6. 1D reaction-diffusion model

We used a one-dimensional (1D) model of steady-state diffusion of CO_2 between an infinite source and a sink to represent rubisco-catalyzed entry of CO_2 into the Calvin-Benson cycle (Fig. S7). A fixed distance, L, separates the CO_2 source and enzymatic sink. Both diffusion and the sink reaction are isotopically selective according to $\varepsilon_{diffusion}$ and ε_{fix}, respectively (Table S2). Here, ε_{fix} refers to the kinetic fractionation factor associated with rubisco (= $\varepsilon_{rubisco}$). Steady-state diffusion in 1D is described by:

(9) $$D \times \frac{d^2C}{dz^2} = 0,$$

where D is the diffusion coefficient, C is the concentration of dissolved CO_2 (=$^{13}CO_2$ + $^{12}CO_2$), and z is the distance coordinate between source and sink. Eq. 9 is subject to the boundary conditions at the edges of the domain $0 \leq z \leq L$:

(10) $$C(z = 0) = C_0$$

(11) $$-D \times \frac{dC}{dz}(z = L) = J_{fix}$$

C_0 represents the initial concentration of $CO_{2(aq)}$, and J_{fix} (=C_{fix}/[SA×f_{SA}]; Table S2) represents the carbon fixation rate normalized to the fraction (f_{SA}) of the surface area (SA) of the cell available to CO_2 transport. The final solution for C as a function of distance has the form:

(12) $$C(z) = C_0 - \frac{J_{fix}}{D} \times z$$

In this expression, C_0 is in units of μg μm^{-3}, D is in units of $\mu m^2\ s^{-1}$, z is in units of μm and J_{fix}, is in units of μg C $\mu m^{-2}\ s^{-1}$. The per-cell carbon fixation rates reflected in J_{fix} are calculated by dividing the measured carbon fixation rates in μg C $cell^{-1}\ s^{-1}$ by the surface area of a cell, which we define as a rod with a radius of 0.5 μm and a length of 2 μm, as well as the fraction of the surface area of the cell available to CO_2 transport. (Table S2).

Similar equations apply for the heavy isotope (^{13}C):

(13) $$^{13}D \times \frac{d^2}{dz^2}(^{13}C) = 0$$

Eq. 13 is subject to the boundary conditions at the edges of the domain $0 \leq z \leq L$:

(14) $$^{13}C(z = 0) = {}^{13}C_0$$

(15) $$-{}^{13}D \times \frac{d^{13}C}{dz}(z = L) = {}^{13}J_{fix}$$

The final solution for ^{13}C as a function of distance has the form:

(16) $$^{13}C(z) = {}^{13}A + {}^{13}B \times z$$

^{13}A and ^{13}B are integration constants defined by the boundary conditions such that

(17) $$^{13}A = {}^{13}C_0$$

(18) $$-{}^{13}D \times {}^{13}B = {}^{13}J_{fix}.$$

We defined ${}^{13}J_{fix}$ through:

(19) $$\alpha_{fix} = \frac{{}^{13}J_{fix}}{{}^{12}J_{fix}} \Big/ \frac{{}^{13}C_L}{{}^{12}C_L}$$

Here α_{fix} is the fractionation factor associated with CO_2 fixation by rubisco (Table S2), while ${}^{13}C_L$ and ${}^{12}C_L$ represent the concentrations of each isotopologue of CO_2 at z = L. Applying the trace isotope abundance approximation ($C_L \approx {}^{12}C_L$, $J_{fix} \approx {}^{12}J_{fix}$) leads to:

(20) $${}^{13}J_{fix} = \alpha_{fix} \times J_{fix} \times \frac{{}^{13}C_L}{C_L}.$$

We combined Eqs. 18 and 20

(21) $$-{}^{13}\mathrm{D} \times {}^{13}\mathrm{B} = \alpha_{\mathrm{fix}} \times \mathrm{J}_{\mathrm{fix}} \times \frac{{}^{13}\mathrm{C}_\mathrm{L}}{\mathrm{C}_\mathrm{L}}$$

to solve for ^{13}B:

(22) $${}^{13}\mathrm{B} = -\frac{\alpha_{fix}\frac{J_{fix}}{D}{}^{13}C_0}{\alpha_{diff}C_L + \alpha_{fix}\frac{J_{fix}}{D}L}$$

Here α_{diff} is the fractionation factor associated with CO_2 diffusion to the site of fixation, which is defined as $\alpha_{diff} = {}^{13}D/{}^{12}D$ (Table S2). The final solution for ^{13}C is then:

(23) $${}^{13}C(z) = {}^{13}C_0\left(1 - \frac{\alpha_{fix}\frac{J_{fix}}{D}}{\alpha_{diff}C_L + \alpha_{fix}\frac{J_{fix}}{D}L}z\right).$$

We then calculated ε_P as the difference between the carbon isotopic composition of fixed carbon and dissolved CO_2 using:

(24) $$\varepsilon_P = \frac{\left(\frac{{}^{13}C_0}{{}^{12}C_0} - \alpha_{fix}\frac{{}^{13}C_L}{{}^{12}C_L}\right)}{\frac{{}^{13}C_0}{{}^{12}C_0}} \times 1000.$$

Independent model inputs are: the carbon fixation rates observed for the Δ*ccm* mutant grown under 1% and 3% CO_2 headspace, the concentration of dissolved CO_2 calculated from pCO_2 and the culture pH using the csys program (*72*), and the fractionation factor for diffusion of CO_2 in water ($\varepsilon_{diff} = [\alpha_{diff} - 1] \times 1000$; Table S2). Two previously published values of the fractionation factor for form IB rubisco ($\varepsilon_{fix} = [\alpha_{fix} - 1] \times 1000$) in cyanobacteria are 22 ± 0.2‰ (*74*) and 20.9 ± 0.8 (*75*), both measured on rubisco from in *Synechococcus* PCC 6301. Here, we set ε_{fix} at 24.3‰, the maximum whole-cell ε_P value we observed for *Synechococcus* 7002.

The model has three free physiological parameters: i) the intracellular distance over which $CO_{2(aq)}$ diffuses (z); ii) the intracellular diffusion coefficient for $CO_{2(aq)}$ (D); and iii) the proportion of cellular surface area available for diffusion (f_{SA}). Free parameters covary over the constrained ranges in Table S2. We trained the model by selecting the interdependent parameter sets that were able reproduce experimental ε_P values observed in the *Synechococcus* 7002 Δ*ccm* mutant (within the ≈0.65‰ data spread for a given experimental condition) at carbon fixation rates observed for both 1% and 3% headspace CO_2 (36 and 107 PAL, respectively). We then continued calculations and model predictions incorporating all interdependent parameter sets [z, D, fSA] that could reproduce experimental ε_P values.

In order to apply the 1D reaction-diffusion model across varying CO_2 levels, we incorporated a previously published model of carbon fixation rate (*76*):

(25) $$C_{fix} = \frac{k_{cat} N_{sites} C}{C + K_{m,CO_2}\left(1 + \frac{O}{K_{m,O_2}}\right)}$$

Here, C_{fix} represents the carbon fixation rate as a function of CO_2 (C) and O_2 (O) concentrations and rubisco kinetic parameters (values listed in Table S2). We fit this theoretical relationship through the observed range of carbon fixation rates using the kinetic parameters for Form IB rubisco in *Synechococcus* 7002 and number of rubisco sites per cell as $N_{sites} = 2.3\times10^5$-$3.4\times10^5$ (Fig. S8). However, this fit could be similarly achieved by scaling the rubisco kinetics to account for differences between calculated and measured carbon fixation rates. The trained dependence of carbon fixation rate on CO_2 concentration is then used as a model input to predict ε_P values at varying CO_2 and O_2 levels (Fig 2B). Modeled ε_P values increase with CO_2 concentration (Fig. S8). Values of ε_P show a greater dependence on carbon fixation at low CO_2 concentrations (Fig. S8B).

The trained model and corresponding carbon fixation rate calculation can then be used to predict ε_P values for a cyanobacterium without a carboxysome grown under varying CO_2 and O_2 conditions with independently derived kinetic parameters for rubisco (see next section).

7. Evolutionary changes in rubisco kinetics

The Δ*ccm* model exercise suggests that, without a CCM, fractionation by extant cyanobacteria with Form IB rubisco can only explain a limited portion of estimated middle Proterozoic ε_P values. The Δ*ccm* model incorporates the kinetics and fractionation for modern Form 1B rubisco (Table S2). Here, we explore how evolutionary changes in rubisco kinetics could impact these modeling results.

Ancesteral sequence reconstruction of Form IA and Form IB rubisco suggest that the kinetics of ancestral Form I rubiscos differed from modern rubisco, although the timing of these evolutionary changes remain unconstrained (*42*). For example, k_{cat} and $K_{m, CO2}$ values for ancestral rubiscos are ~40-80% of modern forms (*42*). While fractionation factors for these reconstructed rubisco (ε_{fix}) forms have not yet been characterized, the kinetics constrain how far ε_P values can deviate from a maximum ε_{fix} value and thus constrain the overall range of ε_P values accessible for a given ε_{fix} value. Substituting the kinetics associated with ancestral Form 1A and Form 1B rubisco, while keeping the rest of the model inputs constant, results in a 7-8‰ range in ε_P values for any given value of ε_{fix} for rubisco (Fig. S9). This range is less than half the 95th percentile range (≈16‰) from our resampling of the mid-Proterozoic carbon isotope record suggesting that, regardless of the ancestral rubisco ε_{fix} value, net carbon isotope fractionation by cyanobacteria with these ancestral rubisco forms could not be responsible for the entire range of mid-Proterozoic ε_P estimates.

We additionally used the measured characteristics of different extant rubisco forms to determine the possible constraints imposed on ε_P by the relationship between kinetics and fractionation factors in cyanobacteria without a CCM. Model sensitivity runs based on paired inputs of rubisco kinetics compiled in (*51*) and fractionation factors compiled in (*77*) show the ε_P ranges accessed by Form 1A , Form 1B, and Form II rubiscos in cyanobacteria without a CCM (Fig. S9, Table S3). Similar to the results with the Δ*ccm* mutant reported here, Form 1B rubiscos in extant cyanobacteria without a CCM can only reproduce a limited range of mid-Proterozoic ε_P values (Fig. S9). If Form II rubisco operated in cyanobacteria without a CCM it would be consistent with a similar range of estimates, while Form 1A rubisco would produce a much smaller range of ε_P values (Fig. S9). Only the kinetics and fractionation factors of Form 1B rubisco from higher plants (*Spinacia oleracea* and *Nicotiana tabacum*) produce ε_P ranges larger than the middle Proterozoic estimates, if they operated in cyanobacteria without a CCM (Fig. S9).

Form 1B rubiscos within extant higher green plants, such as the rubiscos found in *Spinacia oleracea* and *Nicotiana tabacum*, have kinetic parameters and $\varepsilon_{rubisco}$ values that yield substantially larger ranges of ε_P values when incorporated in the 1-D reaction-diffusion model developed for the Δ*ccm* mutant of *Synechococcus* sp. 7002. This suggests that, if middle Proterozoic cyanobacteria contained rubiscos resembling Form 1B in higher green plants, a CCM would not be required to produce the full distribution of middle Proterozoic ε_P values. Archaeplastida are extant representatives of a primary endosymbiotic event, in which an original plastid, derived from an ancestral cyanobacterium, was incorporated into a eukaryotic host cell at ≈1.3 Ga (*21*). Although it is possible that the kinetics of Form 1B rubiscos from Archaeplastida are a vestigial remnant of this ancient endosymbiotic event, it seems unlikely that the selective environment provided by the early Proterozoic surface ocean was similar enough to that within green plant chloroplasts to maintain enzymatic stasis over the ensuing billion years. Altogether, this consideration of potential ancestral rubisco kinetics suggests that carbon isotope fractionation by cyanobacteria lacking a CCM is inconsistent with the estimated distribution of Proterozoic ε_P values.

Supplementary Figures and Tables

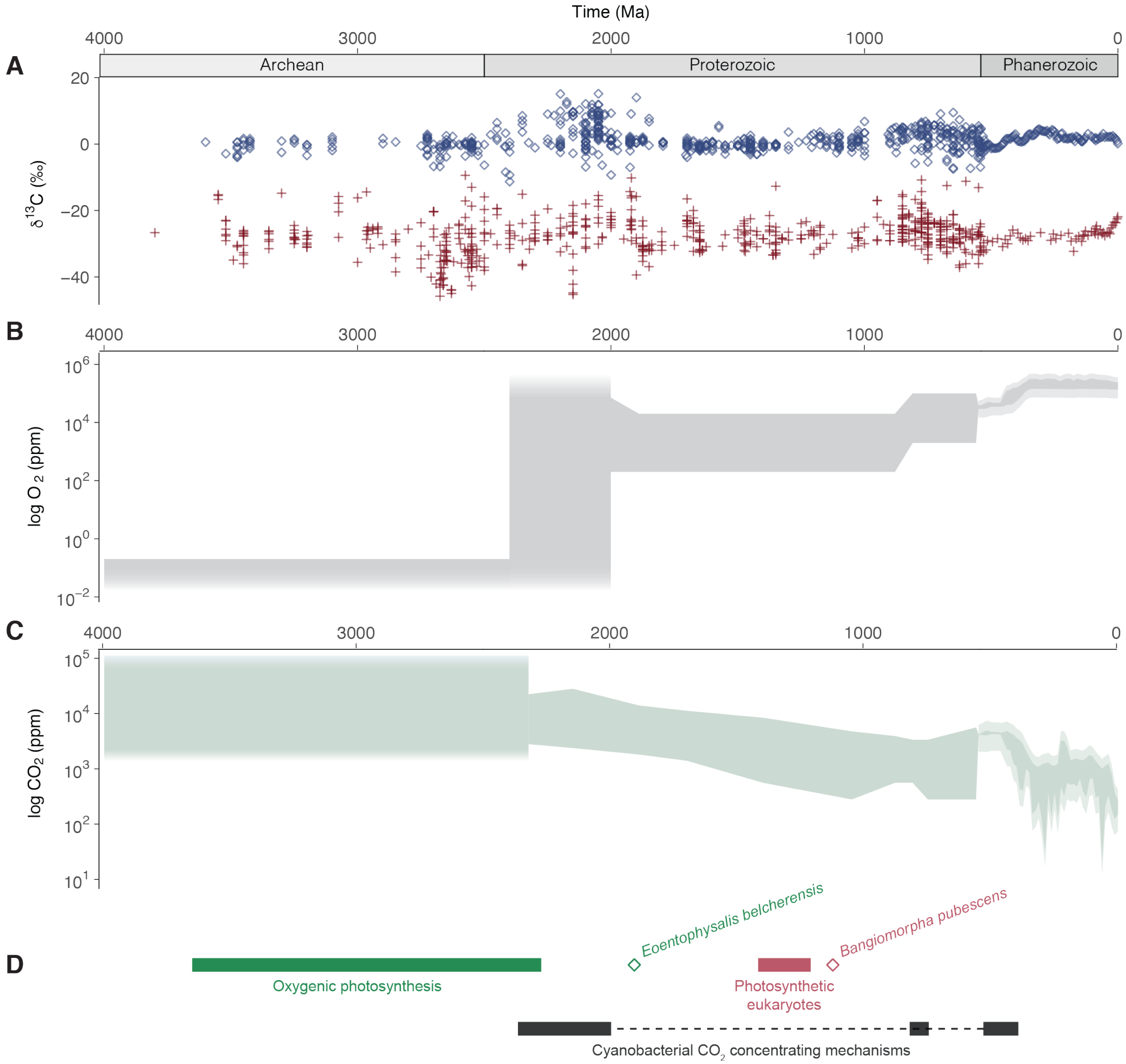

Fig. S1. The carbon isotope record and estimated atmospheric and biologic changes through Earth history. **A.** Values of $\delta^{13}C$ from carbonate minerals (blue) and $\delta^{13}C$ values of total organic carbon (red) are compiled in Krissansen-Totton et al., (*24*). **B.** Archean O_2 estimates restrict pO_2 to $< 10^{-6}$ present atmospheric levels or 2 ppm (*4*). Proterozoic O_2 estimates are compiled in Crockford et al., (*8*). Phanerozoic O_2 estimates come from proxies and modeling (*59*). **C.** Archean CO_2 estimates are from Halevy and Bachan (*39*). Proterozoic CO_2 estimates are compiled in Crockford et al., (*8*). Phanerozoic CO_2 estimates come from proxies and modeling (*59*). **D.** Range of estimates for the origin of oxygenic photosynthesis shown as a green bar (*2*, *3*) and the earliest unambiguous cyanobacterial microfossils (*Eoentophysalis belcherensis*) shown as a green diamond (*13*, *14*). Earliest unambiguous fossil photosynthetic eukaryote (*Bangiomorpha pubescens*) shown as red diamond with corresponding molecular clock estimates for the primary plastid endosymbiosis shown as a red bar (*21*). Proposed dates for the emergence of a cyanobacterial CO_2 Concentrating Mechanism shown as black bars (e.g., *34*).

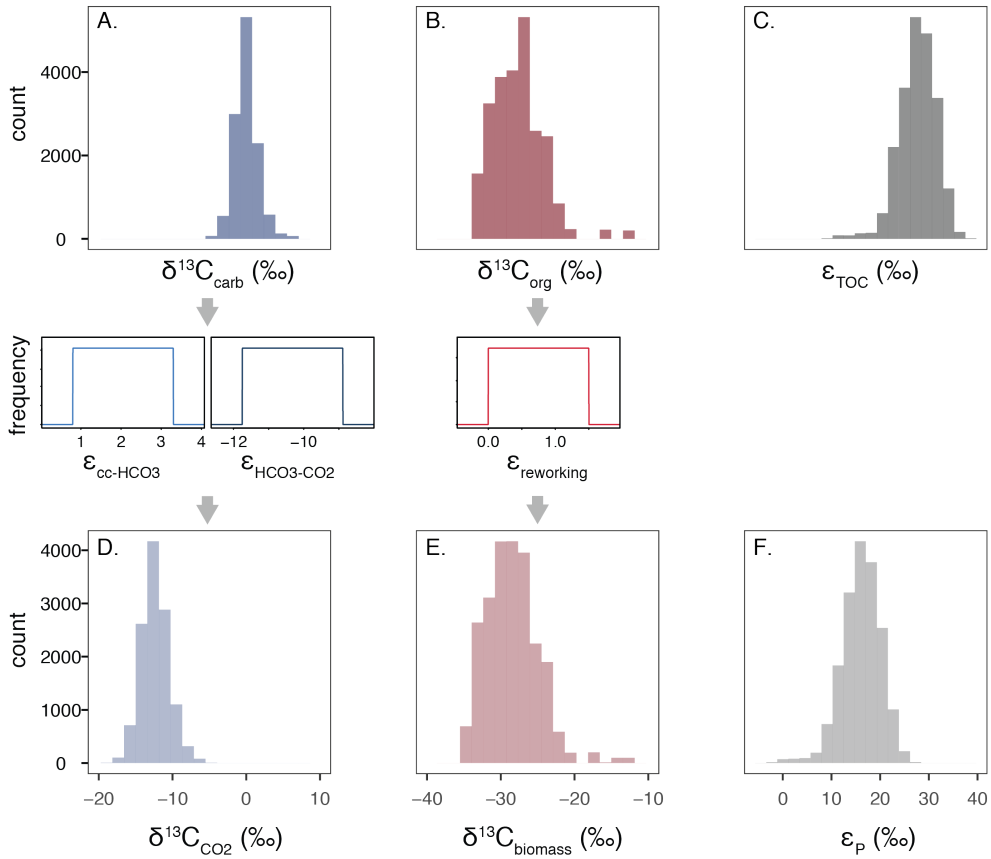

Fig. S2. Representation of bootstrap resampling and Monte Carlo simulations. **A.** Resampled $\delta^{13}C$ values of carbonates and **B.** organic carbon during the non-transitional period between 1.0-1.8 Ga from Krissansen-Totton et al. (*24*). **C.** The distribution of ε_{TOC} values from the bootstrap resampling, calculated according to Eq. 1. **D.** The distribution of predicted $\delta^{13}C$ values of dissolved CO_2, calculated by incorporating the isotope effects associated with precipitation of calcite or aragonite from HCO_3^- and the conversion between HCO_3^- and dissolved CO_2 (inset uniform distributions $\varepsilon_{cc\text{-}HCO3}$ and $\varepsilon_{HCO3\text{-}CO2}$). **E.** The distribution of predicted $\delta^{13}C$ values of primary biomass calculated by incorporating an isotope effect associated with secondary reworking in the water column and sediments (inset uniform distribution $\varepsilon_{reworking}$). **F.** The distribution of predicted ε_P values calculated according to Eq. 2. See text for simulation details.

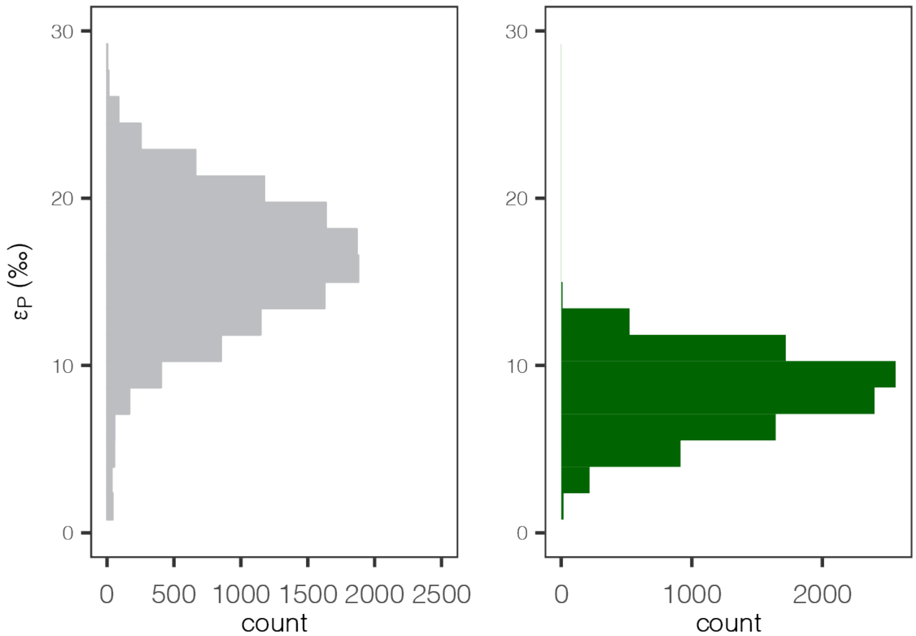

Fig. S3. Comparing the ε_P distribution between the middle Proterozoic (left) and a modern cyanobacterial mat (right). Both distributions are the result of Monte Carlo simulations and bootstrap resampling of sedimentary carbon isotope records (left) and a previously published isotopic characterization of a cyanobacterial mat (right; *26*).

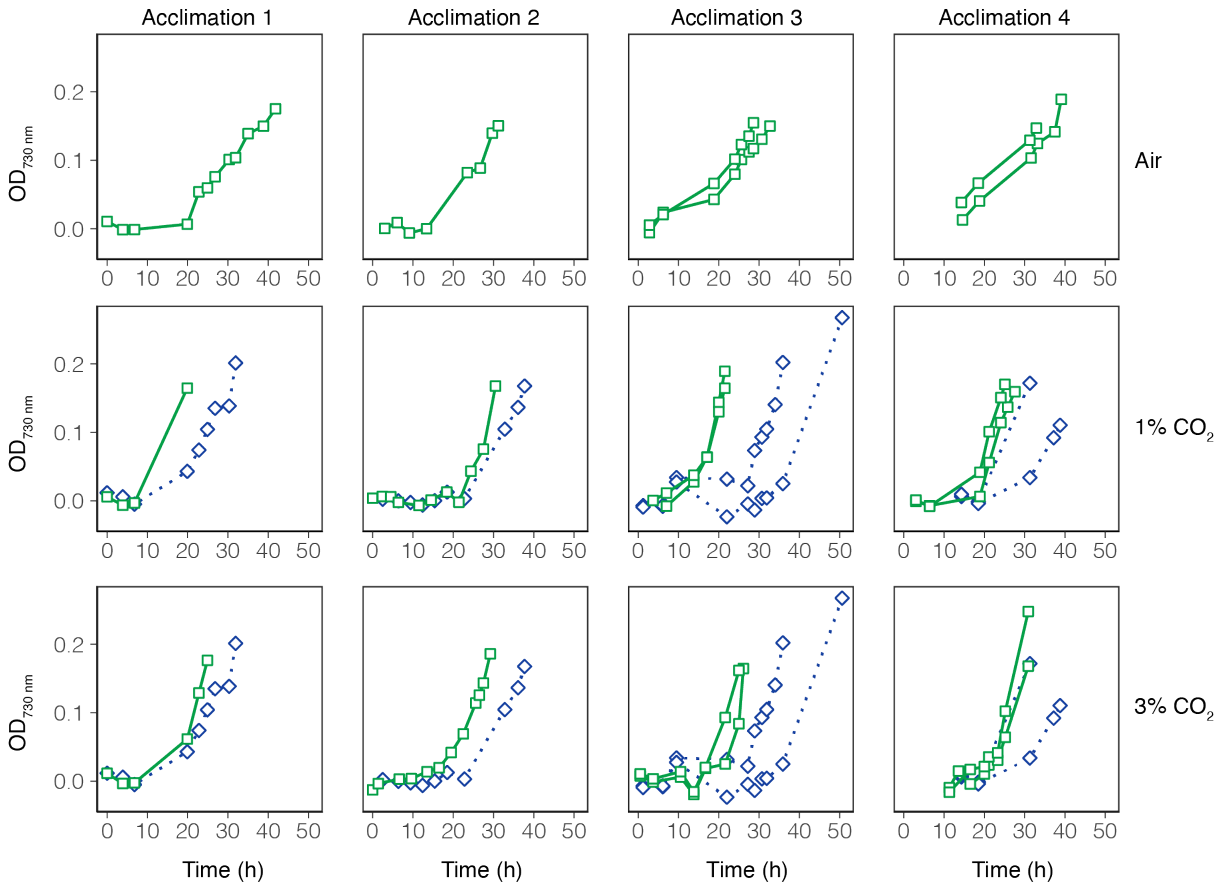

Fig. S4. Growth curves for cultures of *Synechococcus* 7002 in air, 1% CO_2, and 3% CO_2 corresponding to 1, 36, and 107 PAL CO_2. Green squares and solid lines represent wild-type *Synechococcus* 7002. Blue diamonds and dashed lines represent the Δ*ccm* mutant.

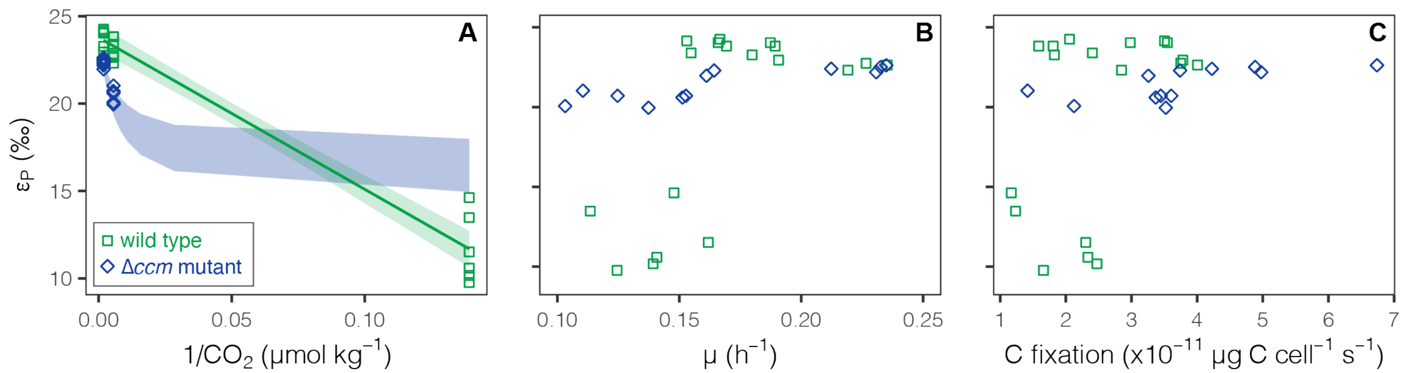

Fig. S5. The dependence of ε_P values observed in *Synechococcus* 7002 cultures on CO_2 and growth parameters. **A.** Values of ε_P in the wild-type strain (green symbols) show a linear dependence on $1/CO_2$ (green line; R^2: 0.96, shading represents 95% confidence interval). Values of ε_P in the Δ*ccm* strain (blue symbols) were used to model the dependence of ε_P on CO_2 concentration (blue shading). **B.** Values of ε_P do not vary systematically with specific growth rate (μ). **C.** The relationship between carbon fixation rate and ε_P values used to train the Δ*ccm* strain model.

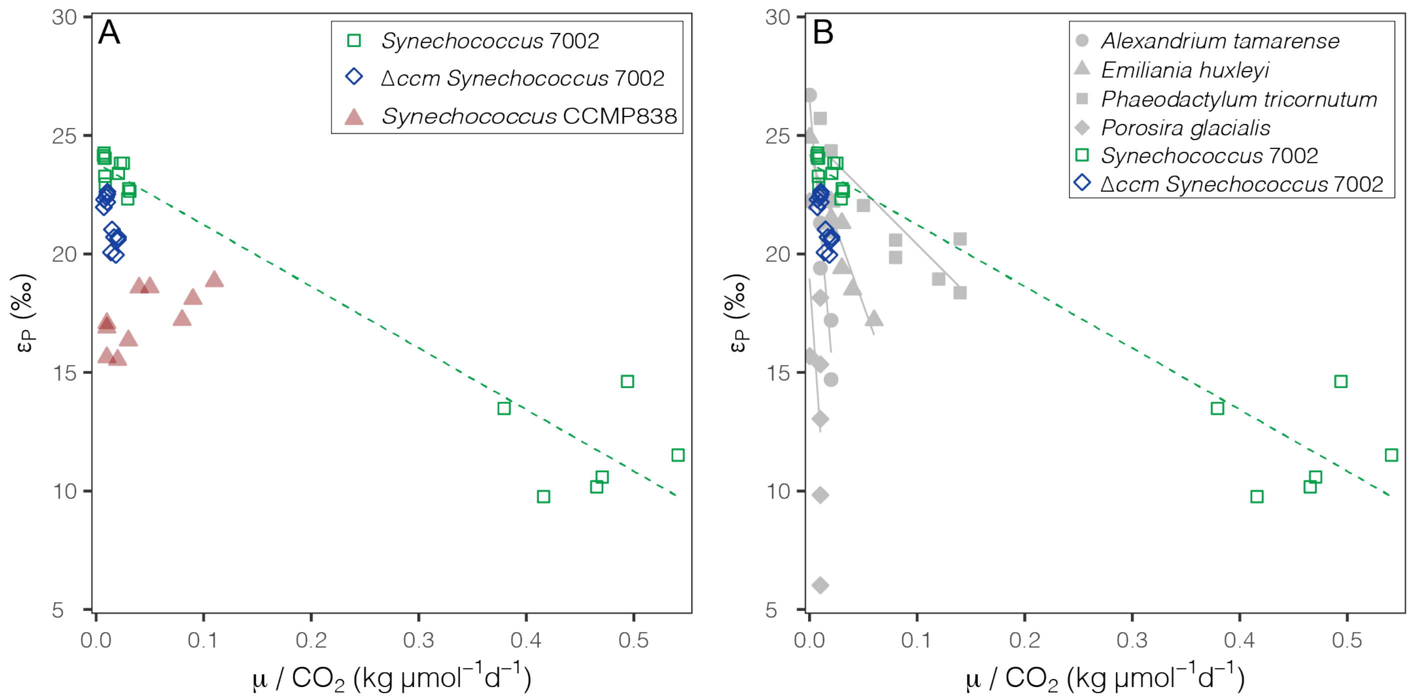

Fig. S6. Cyanobacterial and algal ε_P relationships. **A**. Cyanobacterial ε_P relationships observed in wild-type *Synechococcus* 7002 and Δ*ccm* mutant (this study) differ from the ε_P relationship found in alpha cyanobacterium Synechoccus CCMP838 (*28*). **B**. ε_P relationships found in wild type *Synechococcus* 7002 and Δ*ccm* mutant resemble ε_P relationships in eukaryotic algae (*78*).

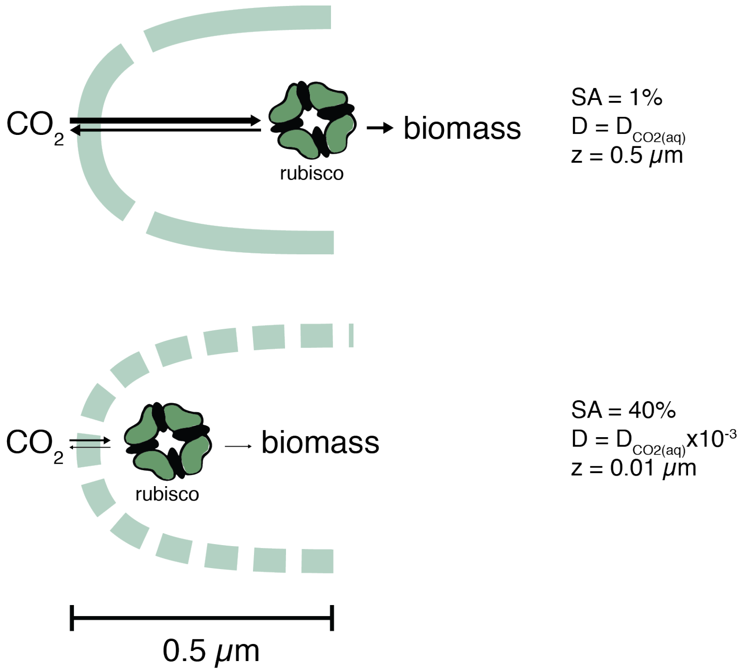

Fig. S7. 1D reaction-diffusion model. Fluxes include diffusion of CO_2 into the cell, autotrophic carbon fixation through the Calvin-Benson cycle, and diffusion of CO_2 out of the cell. The three interdependent model parameters are the surface area available for diffusion of CO_2 (SA), the diffusion coefficient for CO_2 at 37°C (D), and the distance to the rubisco active site (z). Example values of these parameters are shown here to illustrate the range of values possible for each parameter.

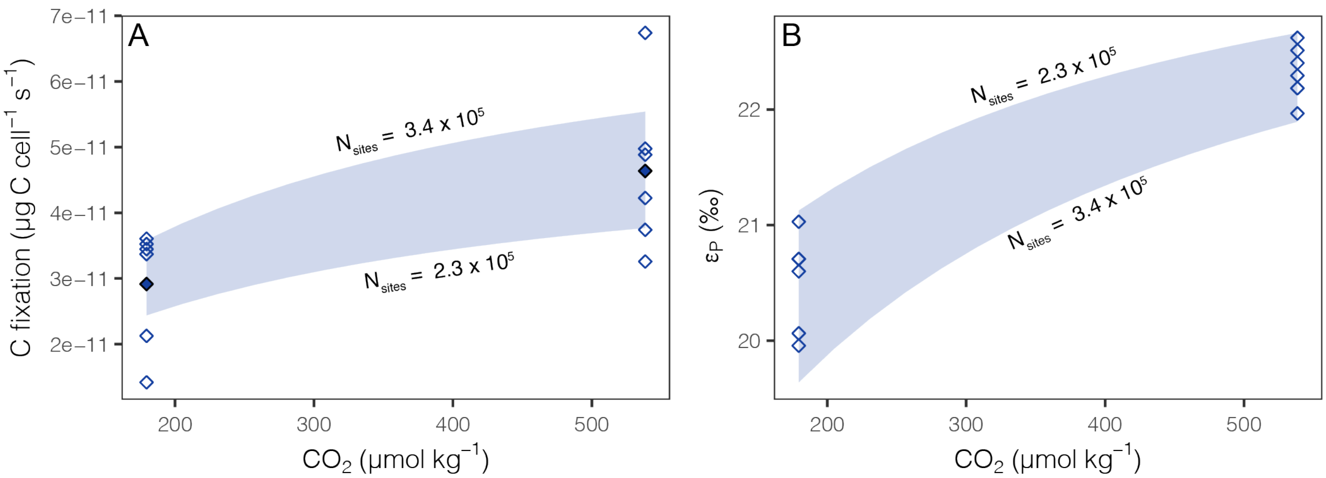

Fig. S8. Carbon fixation rate and ε_P values as a function of dissolved CO_2 concentration in the Δ*ccm* mutant. **A:** Open symbols represent measured carbon fixation rate for cultures of the Δ*ccm* mutant grown under a 1% and 3% CO_2 headspace (36 and 107 PAL CO_2). The shaded area represents the theoretical relationship between carbon fixation rate and CO_2 concentration from Clark et al. (*76*) fit to the observed culture data using the number of rubisco sites (N_{sites}). This fit could be similarly achieved by scaling the rubisco kinetics or incorporating an unknown factor to account for differences between the theoretical model and the measured carbon fixation rates. **B:** The carbon fixation rate as a function of dissolved CO_2 concentration is then used as a model input to predict corresponding ε_P values.

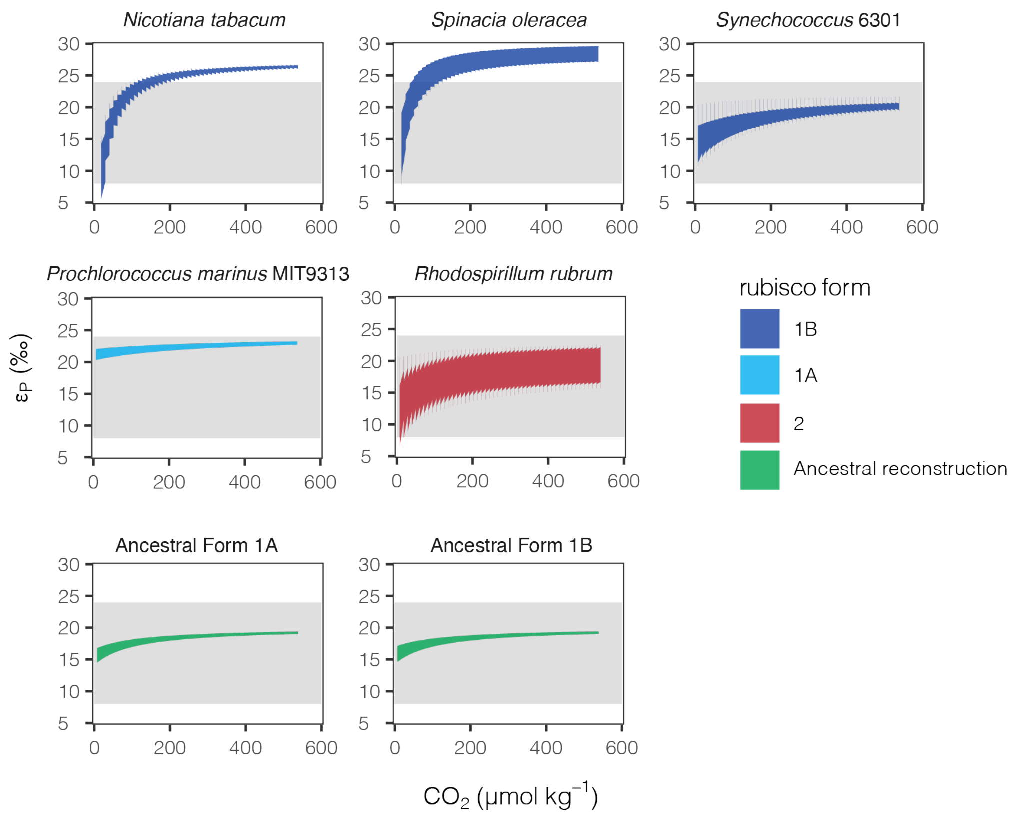

Fig. S9. The modeled relationship between ε_P values and CO_2 for both extant rubisco and ancestral reconstructions. The grey band represents the estimated middle Proterozoic distribution of ε_P (95^{th} percentile; 8-24‰). For extant rubisco forms, colored fields represent model results with ε_{fix} values from (*77*) and rubisco kinetics from (*51*) listed in Table S3. For the ancestral forms, colored fields represent model results with an example ε_{fix} value of 20‰ and kinetic parameters from (*42*). In all cases the model was run over O_2 concentrations of 0.14-14 μmol l^{-1} (0.1-10% PAL).

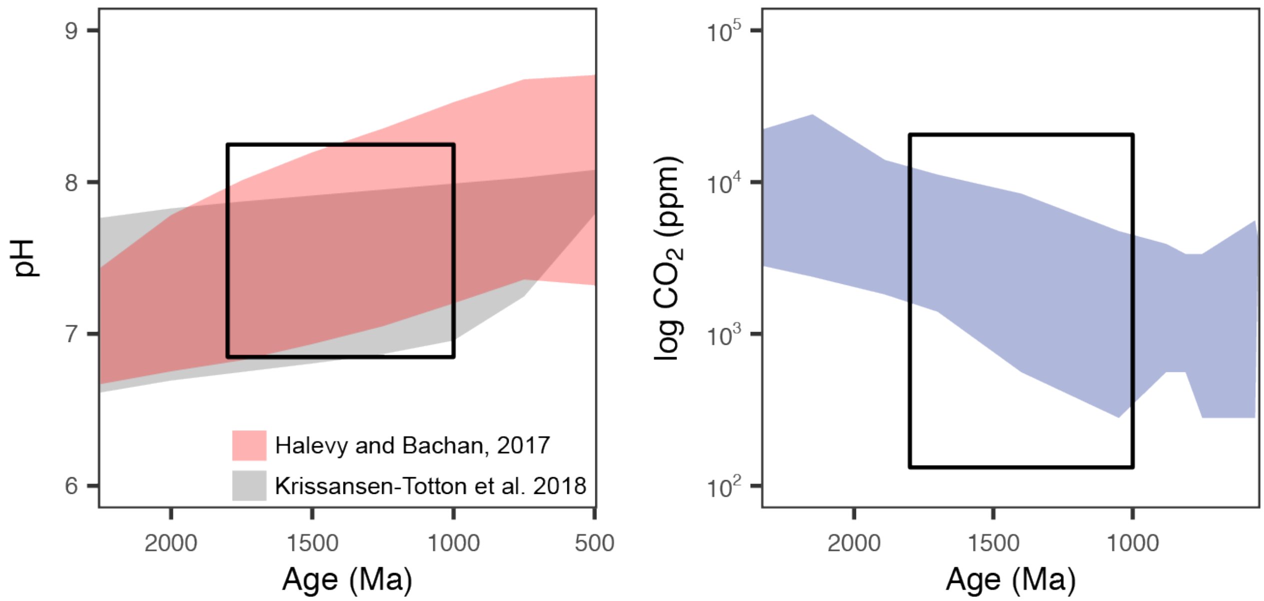

Fig. S10. Experimental culture conditions projected onto Proterozoic pCO_2 and pH estimates. The height of the boxes represents the experimental range of pH (left) and dissolved CO_2 translated into pCO_2 levels using the culture pH between assumed Proterozoic ocean temperatures of 3-30°C (right). The width of the box represents the middle Proterozoic time period resampled for the statistical simulations of the carbon isotope record. Estimates of Proterozoic pH are 95% confidence intervals from (*39*) and (*38*). Estimates of Proterozoic pCO_2 levels are from (*8*).

Supplementary Table 1. Growth parameters for wild type *Synechococcus* 7002 and Δ*ccm* mutant. Net specific growth rate was calculated according to Eq. S6. Carbon fixation rates (C_{fix}) was calculated according to Eq. S7. Analytical error for $\delta^{13}C_{biomass}$ values is ±0.1‰ and 0.01‰ for $\delta^{13}C_{CO2}$ values. Values of $\delta^{13}C_{CO2}$ in air are from https://www.esrl.noaa.gov/gmd/dv/iadv/index.php (Niwot Ridge site).

Headspace CO_2 (PAL)	CO_2 (µmol kg^{-1})	Strain	Acclimation	Doubling time (h)	C_{fix} (fg C $cell^{-1}$ h^{-1})	$\delta^{13}C_{biomass}$ (‰)	$\delta^{13}C_{CO2}$ (‰)	ε_P (‰)
1	7	WT	1	6.1	44	-22.5	-8.0	13.5 ± 0.1
1	7	WT	2	4.7	42	-23.5	-8.0	14.6 ± 0.1
1	7	WT	3	4.9	84	-19.6	-8.0	10.6 ± 0.1
1	7	WT	3	4.3	83	-20.4	-8.0	11.5 ± 0.1
1	7	WT	4	5.6	60	-18.7	-8.0	9.8 ± 0.1
1	7	WT	4	5.0	89	-19.1	-8.0	10.2 ± 0.1
36	180	WT	1	3.0	144	-50.2	-27.7	22.6 ± 0.1
36	180	WT	2	4.5	87	-50.8	-27.7	23.4 ± 0.1
36	180	WT	3	3.1	135	-50.1	-27.7	22.7 ± 0.1
36	180	WT	3	3.2	103	-49.8	-27.7	22.3 ± 0.1
36	180	WT	4	4.1	65	-51.1	-27.7	23.8 ± 0.1
36	180	WT	4	3.7	57	-51.1	-27.7	23.8 ± 0.1
107	538	WT	1	3.6	136	-63.0	-40.6	22.9 ± 0.1
107	538	WT	2	4.2	107	-63.9	-40.6	24.0 ± 0.1
107	538	WT	3	3.9	66	-63.1	-40.6	23.3 ± 0.1
107	538	WT	3	3.7	128	-63.8	-40.6	24.0 ± 0.1
107	538	WT	4	4.5	126	-63.8	-40.6	24.1 ± 0.1
107	538	WT	4	4.2	74	-63.9	-40.6	24.3 ± 0.1
36	180	Δ*ccm*	1	4.5	130	-48.3	-27.7	20.7 ± 0.1
36	180	Δ*ccm*	2	5.6	124	-48.3	-27.7	20.7 ± 0.1
36	180	Δ*ccm*	3	5.1	127	-47.5	-27.7	20.0 ± 0.1
36	180	Δ*ccm*	3	6.7	77	-47.7	-27.7	20.1 ± 0.1
36	180	Δ*ccm*	4	4.6	121	-48.0	-27.7	20.6 ± 0.1
36	180	Δ*ccm*	4	6.3	51	-48.4	-27.7	21.0 ± 0.1
107	538	Δ*ccm*	1	4.2	135	-62.4	-40.6	22.3 ± 0.1
107	538	Δ*ccm*	2	4.3	117	-61.9	-40.6	22.0 ± 0.1
107	538	Δ*ccm*	3	3.3	152	-62.2	-40.6	22.4 ± 0.1
107	538	Δ*ccm*	3	3.0	179	-62.1	-40.6	22.2 ± 0.1
107	538	Δ*ccm*	4	3.0	176	-62.3	-40.6	22.5 ± 0.1
107	538	Δ*ccm*	4	3.0	243	-62.3	-40.6	22.6 ± 0.1

Supplementary Table 2. 1D reaction-diffusion model parameters.

Parameter	Description	Values	Units	Notes
C_{fix}	Measured C fixation rate	1.4×10^{-11}-6.7×10^{-11}	$\mu g\ C\ cell^{-1}\ s^{-1}$	Grown under 25-75 PAL CO_2
J_{fix}	Converted C fixation rate		$\mu g\ C\ \mu m^{-2}\ s^{-1}$	Cfix/(SA × fSA)
C_0	Experimental dissolved [CO_2]	8.8×10^{-14}-6.6×10^{-12}	$\mu g\ C\ \mu m^{-3}$	Calculated from *p*CO2 and pH using csys (*72*)
z	Distance to the sink	0.01-0.5	µm	Based on a cell with a radius of 0.5 µm
SA	Surface area of a rod	6.3	μm^2	Based on a rod with a radius of 0.5 µm and a length of 2 µm representing a cyanobacterial cell
fSA	Effective surface area	0.01-0.4	fraction	Proportion of surface area available for diffusion of CO_2
D	Diffusion coefficient CO_2	26.9-2690	$\mu m^2\ s^{-1}$	Constrained by the diffusion coefficient of $CO_{2(aq)}$ in water ($2.69 \times 10^3\ \mu m^2\ s^{-1}$ at 37°C) (*79*)
α_{diff}	Fractionation associated with diffusion of CO_2	1.00087		O'Leary et al. (*80*)
α_{fix}	Fractionation associated with rubisco	1.0243		Note 1.
k_{cat}	form IB rubisco	11.4	$molecules\ site^{-1}\ s^{-1}$	adapted from Clark et al. (*76*)
K_{m,CO_2}	form IB rubisco	185	$\mu mol\ l^{-1}$	adapted from Clark et al. (*76*)
K_{m,O_2}	form IB rubisco	1300	$\mu mol\ l^{-1}$	adapted from Clark et al. (*76*)
O_2	Concentration of dissolved O_2	143	$\mu mol\ l^{-1}$	Calculated. Note 2.
N_{sites}	rubisco active sites	2.3×10^5-3.4×10^5	number	Note 3.

[1] Previously published fractionation for form IB rubisco in *Synechococcus* PCC 6301 are 22 ± 0.2‰ (*74*) and 20.9 ± 0.8 (*75*). Here, we set ε_{fix} at 24.3‰, the maximum whole-cell ε_P value we observed for *Synechococcus* 7002.

[2] The concentration of dissolved oxygen was calculated from DOTABLES from the USGS (https://www.usgs.gov/software/dotables) using growth medium conditions of 37°C, 0.821 atm, and 32‰ salinity.

[3] The number of rubisco active sites was used to fit the theoretical relationship (*76*) through the observed range of carbon fixation rates at 36 and 107 PAL. This fit could be similarly achieved by scaling the rubisco kinetics.

Supplementary Table 3. Model inputs for rubisco characteristics from extant organisms and ancestral state reconstructions (ASR). Values for ε_{fix} from (*77*), kinetic parameters for extant rubiscos from (*51*), kinetic parameters for ancestral rubiscos from (*42*)

Source	Form	ε_{fix}	k_{cat} (s^{-1})			$K_{m\,CO2}$ (μM)			$K_{m\,O2}$ (μM)			Taxonomy
ASR	Anc. 1B	--	4.77	±	0.1	113	±	6	2010	±	571	Ancestral
ASR	Anc. 1A	--	4.72	±	0.1	120	±	10	641	±	49	Ancestral
Spinacia oleracea	1B	29.3	2.9	±	0.2	10	±	1	250	±	33	C3 plants
Spinacia oleracea	1B	29.3	3.2	±	0.1	12.1	±	1	574	±	19	C3 plants
Spinacia oleracea	1B	29.3	3.2	±	0.1	12.1	±	1	574	±	19	C3 plants
Spinacia oleracea	1B	29.3	2.7	±	0.1	11	±	2	520	±	25	C3 plants
Nicotiana tabacum	1B	27.4	3.9	±	0.2	9	±	0	292	±	20	C3 plants
Nicotiana tabacum	1B	27.4	3.4	±	0.1	10.7	±	1	295	±	71	C3 plants
Nicotiana tabacum	1B	27.4	3.1	±	0.3	9.7	±	0	283	±	15	C3 plants
Nicotiana tabacum	1B	27.4	3.4	±	0.1	10.7	±	1	295	±	71	C3 plants
Synechococcus 6301	1B	22.0	11.4	±	0.7	185	±	17	1300	±	172	Cyanobacteria
Synechococcus 6301	1B	22.0	12	±	0.7	167	±	15	529	±	69.8	Cyanobacteria
Synechococcus 6301	1B	22.0	11.8	±	0.2	200	±	9	199	±	42	Cyanobacteria
Synechococcus 6301	1B	22.0	2.57	±	0.2	142	±	1	664	±	82	Cyanobacteria
Synechococcus 6301	1B	22.0	3.71	±	0.2	167	±	2	529	±	14	Cyanobacteria
Synechococcus 6301	1B	22.0	11.6	±	0.4	340	±	12	972	±	26	Cyanobacteria
Synechococcus 6301	1B	22.0	9.78	±	0.5	152	±	23	1230	±	135	Cyanobacteria
Prochlorococcus marinus MIT9313	1A	24.0	6.58	±	0.3	309	±	24	1400	±	300	Cyanobacteria
Rhodospirillum rubrum	2	20.4	5.7	±	0.3	89	±	8	406	±	53.6	Alphaproteobacteria
Rhodospirillum rubrum	2	20.4	12.3	±	0.3	149	±	8	159	±	25	Alphaproteobacteria
Rhodospirillum rubrum	2	20.4	4.3	±	0.5	125	±	12	143	±	3	Alphaproteobacteria
Rhodospirillum rubrum	2	20.4	7.3	±	0.3	80	±	11	406	±	48	Alphaproteobacteria

REFERENCES AND NOTES

1. D. E. Canfield, The early history of atmospheric oxygen: Homage to Robert M. Garrels. *Annu. Rev. Earth Planet. Sci.* **33**, 1–36 (2005).
2. W. W. Fischer, J. Hemp, J. E. Johnson, Evolution of oxygenic photosynthesis. *Annu. Rev. Earth Planet. Sci.* **44**, 647–683 (2016).
3. P. Sánchez-Baracaldo, T. Cardona, On the origin of oxygenic photosynthesis and Cyanobacteria. *New Phytol.* **225**, 1440–1446 (2020).
4. D. C. Catling, K. J. Zahnle, The Archean atmosphere. *Sci. Adv.* **6**, eaax1420 (2020).
5. M. S. W. Hodgskiss, P. W. Crockford, Y. Peng, B. A. Wing, T. J. Horner, A productivity collapse to end Earth's Great Oxidation. *Proc. Natl. Acad. Sci. U.S.A.* **116**, 17207–17212 (2019).
6. N. J. Planavsky, C. T. Reinhard, X. Wang, D. Thomson, P. McGoldrick, R. H. Rainbird, T. Johnson, W. W. Fischer, T. W. Lyons, Low mid-Proterozoic atmospheric oxygen levels and the delayed rise of animals. *Science* **346**, 635–638 (2014).
7. P. W. Crockford, J. A. Hayles, H. Bao, N. J. Planavsky, A. Bekker, P. W. Fralick, G. P. Halverson, T. H. Bui, Y. Peng, B. A. Wing, Triple oxygen isotope evidence for limited mid-Proterozoic primary productivity. *Nature* **559**, 613–616 (2018).
8. P. W. Crockford, M. Kunzmann, A. Bekker, J. Hayles, H. Bao, G. P. Halverson, Y. Peng, T. H. Bui, G. M. Cox, T. M. Gibson, S. Wörndle, R. Rainbird, A. Lepland, N. L. Swanson-Hysell, S. Master, B. Sreenivas, A. Kuznetsov, V. Krupenik, B. A. Wing, Claypool continued: Extending the isotopic record of sedimentary sulfate. *Chem. Geol.* **513**, 200–225 (2019).
9. M. A. Kipp, E. E. Stüeken, Biomass recycling and Earth's early phosphorus cycle. *Sci. Adv.* **3**, eaao4795 (2017).
10. S. L. Olson, C. T. Reinhard, T. W. Lyons, Cyanobacterial diazotrophy and Earth's delayed oxygenation. *Front. Microbiol.* **7**, 1526 (2016).
11. C. Scott, T. W. Lyons, A. Bekker, Y. Shen, S. W. Poulton, X. Chu, A. D. Anbar, Tracing the stepwise oxygenation of the Proterozoic ocean. *Nature* **452**, 456–459 (2008).
12. K. Ozaki, K. J. Thompson, R. L. Simister, S. A. Crowe, C. T. Reinhard, Anoxygenic photosynthesis and the delayed oxygenation of Earth's atmosphere. *Nat. Commun.* **10**, 3026 (2019).
13. H. J. Hofmann, Precambrian Microflora, Belcher Islands, Canada: Significance and systematics.s *J. Paleo.* **50**, 1040–1073 (1976).
14. M. S. W. Hodgskiss, O. M. J. Dagnaud, J. L. Frost, G. P. Halverson, M. D. Schmitz, N. L. Swanson-Hysell, E. A. Sperling, New insights on the Orosirian carbon cycle, early Cyanobacteria, and the

assembly of Laurentia from the Paleoproterozoic Belcher Group. *Earth Planet. Sci. Lett.* **520**, 141–152 (2019).

15. L. C. Kah, A. H. Knoll, Microbenthic distribution of Proterozoic tidal flats: Environmental and taphonomic considerations. *Geology* **24**, 79–82 (1996).
16. V. N. Sergeev, M. Sharma, Y. Shukla, Proterozoic fossil cyanobacteria. *Palaeobotanist* **61**, 189–358 (2012).
17. C. F. Demoulin, Y. J. Lara, L. Cornet, C. François, D. Baurain, A. Wilmotte, E. J. Javaux, Cyanobacteria evolution: Insight from the fossil record. *Free Radic. Biol. Med.* **140**, 206–223 (2019).
18. P. Sánchez-Baracaldo, Origin of marine planktonic cyanobacteria. *Sci. Rep.* **5**, 17418 (2015).
19. A. H. Knoll, R. E. Summons, J. R. Waldbauer, J. E. Zumberge, The geological succession of primary producers in the oceans, in *Evolution of Primary Producers in the Sea* (Elsevier, 2007), pp. 133–163.
20. N. Gueneli, A. M. McKenna, N. Ohkouchi, C. J. Boreham, J. Beghin, E. J. Javaux, J. J. Brocks, 1.1-billion-year-old porphyrins establish a marine ecosystem dominated by bacterial primary producers. *Proc. Natl. Acad. Sci. U.S.A.* **115**, E6978–E6986 (2018).
21. T. M. Gibson, P. M. Shih, V. M. Cumming, W. W. Fischer, P. W. Crockford, M. S. W. Hodgskiss, S. Wörndle, R. A. Creaser, R. H. Rainbird, T. M. Skulski, G. P. Halverson, Precise age of *Bangiomorpha pubescens* dates the origin of eukaryotic photosynthesis. *Geology* **46**, 135–138 (2017).
22. J. J. Brocks, A. J. M. Jarrett, E. Sirantoine, C. Hallmann, Y. Hoshino, T. Liyanage, The rise of algae in Cryogenian oceans and the emergence of animals. *Nature* **548**, 578–581 (2017).
23. J. M. Hayes, H. Strauss, A. J. Kaufman, The abundance of ^{13}C in marine organic matter and isotopic fractionation in the global biogeochemical cycle of carbon during the past 800 Ma. *Chem. Geol.* **161**, 103–125 (1999).
24. J. Krissansen-Totton, R. Buick, D. C. Catling, A statistical analysis of the carbon isotope record from the Archean to Phanerozoic and implications for the rise of oxygen. *Am. J. Sci.* **315**, 275–316 (2015).
25. J. Schopf, M. Walter, in *The Biology of Cyanobacteria*, N.G. Carr, B.A. Whitton, eds. (Blackwell, 1982), pp. 543–564.
26. M. Schidlowski, H. Gorzawski, I. Dor, Carbon isotope variations in a solar pond microbial mat: Role of environmental gradients as steering variables. *Geochim. Cosmochim. Acta* **58**, 2289–2298 (1994).

27. D. J. Des Marais, D. E. Canfield, The carbon isotope biogeochemistry of microbial mats, in *Microbial Mats: Structure, Development and Environmental Significance*, L. J. Stal, P. Caumette, Eds. (Springer Berlin Heidelberg, 1994), pp. 289–298.
28. B. N. Popp, E. A. Laws, R. R. Bidigare, J. E. Dore, K. L. Hanson, S. G. Wakeham, Effect of phytoplankton cell geometry on carbon isotopic fractionation. *Geochim. Cosmochim. Acta* **62**, 69–77 (1998).
29. B. D. Rae, B. M. Long, M. R. Badger, G. D. Price, Functions, compositions, and evolution of the two types of carboxysomes: Polyhedral microcompartments that facilitate CO_2 fixation in cyanobacteria and some proteobacteria. *Microbiol. Mol. Biol. Rev.* **77**, 357–379 (2013).
30. T. D. Sharkey, Discovery of the canonical Calvin–Benson cycle. *Photosynth. Res.* **140**, 235–252 (2019).
31. J. C. Cameron, S. C. Wilson, S. L. Bernstein, C. A. Kerfeld, Biogenesis of a bacterial organelle: The carboxysome assembly pathway. *Cell* **155**, 1131–1140 (2013).
32. N. C. Hill, J. W. Tay, S. Altus, D. M. Bortz, J. C. Cameron, Life cycle of a cyanobacterial carboxysome. *Sci. Adv.* **6**, eaba1269 (2020).
33. P. Mahinthichaichan, D. M. Morris, Y. Wang, G. J. Jensen, E. Tajkhorshid, Selective permeability of carboxysome shell pores to anionic molecules. *J. Phys. Chem. B* **122**, 9110–9118 (2018).
34. M. Giordano, J. Beardall, J. A. Raven, CO_2 concentrating mechanisms in algae: Mechanisms, environmental modulation, and evolution. *Annu. Rev. Plant Biol.* **56**, 99–131 (2005).
35. L. Whitehead, B. M. Long, G. D. Price, M. R. Badger, Comparing the in vivo function of α-carboxysomes and β-carboxysomes in two model cyanobacteria. *Plant Physiol.* **165**, 398–411 (2014).
36. G. C. Gordon, T. C. Korosh, J. C. Cameron, A. L. Markley, M. B. Begemann, B. F. Pfleger, CRISPR interference as a titratable, *trans*-acting regulatory tool for metabolic engineering in the cyanobacterium *Synechococcus sp.* strain PCC 7002. *Metab. Eng.* **38**, 170–179 (2016).
37. R. L. Clark, G. C. Gordon, N. R. Bennett, H. Lyu, T. W. Root, B. F. Pfleger, High-CO_2 requirement as a mechanism for the containment of genetically modified cyanobacteria. *ACS Synth. Biol.* **7**, 384–391 (2018).
38. J. Krissansen-Totton, G. N. Arney, D. C. Catling, Constraining the climate and ocean pH of the early Earth with a geological carbon cycle model. *Proc. Natl. Acad. Sci.* **115**, 4105–4110 (2018).
39. I. Halevy, A. Bachan, The geologic history of seawater pH. *Science* **355**, 1069–1071 (2017).

40. E. A. Laws, B. N. Popp, R. R. Bidigare, M. C. Kennicutt, S. A. Macko, Dependence of phytoplankton carbon isotopic composition on growth rate and $[CO_2]_{aq}$: Theoretical considerations and experimental results. *Geochim. Cosmochim. Acta* **59**, 1131–1138 (1995).
41. B. Kacar, V. Hanson-Smith, Z. R. Adam, N. Boekelheide, Constraining the timing of the Great Oxidation Event within the Rubisco phylogenetic tree. *Geobiology* **15**, 628–640 (2017).
42. P. M. Shih, A. Occhialini, J. C. Cameron, P. J. Andralojc, M. A. J. Parry, C. A. Kerfeld, Biochemical characterization of predicted Precambrian RuBisCO. *Nat. Commun.* **7**, 10382 (2016).
43. M. Lebrato, D. Garbe-Schönberg, M. N. Müller, S. Blanco-Ameijeiras, R. A. Feely, L. Lorenzoni, J.-C. Molinero, K. Bremer, D. O. B. Jones, D. Iglesias-Rodriguez, D. Greeley, M. D. Lamare, A. Paulmier, M. Graco, J. Cartes, J. Barcelos e Ramos, A. de Lara, R. Sanchez-Leal, P. Jimenez, F. E. Paparazzo, S. E. Hartman, U. Westernströer, M. Küter, R. Benavides, A. F. da Silva, S. Bell, C. Payne, S. Olafsdottir, K. Robinson, L. M. Jantunen, A. Korablev, R. J. Webster, E. M. Jones, O. Gilg, P. B. du Bois, J. Beldowski, C. Ashjian, N. D. Yahia, B. Twining, X.-G. Chen, L.-C. Tseng, J.-S. Hwang, H.-U. Dahms, A. Oschlies, Global variability in seawater Mg:Ca and Sr:Ca ratios in the modern ocean. *Proc. Natl. Acad. Sci. U.S.A.* **117**, 22281–22292 (2020).
44. K.-H. Tang, Y. Tang, R. E. Blankenship, Carbon metabolic pathways in phototrophic bacteria and their broader evolutionary implications. *Front. Microbiol.* **2**, 165 (2011).
45. L. C. Kah, R. Riding, Mesoproterozoic carbon dioxide levels inferred from calcified cyanobacteria. *Geology* **35**, 799–802 (2007).
46. G. D. Price, M. R. Badger, F. J. Woodger, B. M. Long, Advances in understanding the cyanobacterial CO_2-concentrating-mechanism (CCM): Functional components, Ci transporters, diversity, genetic regulation and prospects for engineering into plants. *J. Exp. Bot.* **59**, 1441–1461 (2008).
47. H. Bauwe, M. Hagemann, A. R. Fernie, Photorespiration: Players, partners and origin. *Trends Plant Sci.* **15**, 330–336 (2010).
48. A. Bachan, L. R. Kump, The rise of oxygen and siderite oxidation during the Lomagundi Event. *Proc. Natl. Acad. Sci. U.S.A.* **112**, 6562–6567 (2015).
49. S. Kihara, D. A. Hartzler, S. Savikhin, Oxygen concentration inside a functioning photosynthetic cell. *Biophys. J.* **106**, 1882–1889 (2014).
50. G. C. Cannon, C. E. Bradburne, H. C. Aldrich, S. H. Baker, S. Heinhorst, J. M. Shively, Microcompartments in prokaryotes: Carboxysomes and related polyhedra. *Appl. Environ. Microbiol.* **67**, 5351–5361 (2001).

51. A. I. Flamholz, N. Prywes, U. Moran, D. Davidi, Y. M. Bar-On, L. M. Oltrogge, R. Alves, D. Savage, R. Milo, Revisiting trade-offs between Rubisco kinetic parameters. *Biochemistry* **58**, 3365–3376 (2019).
52. J. W. Schopf, Disparate rates, differing fates: Tempo and mode of evolution changed from the Precambrian to the Phanerozoic. *Proc. Natl. Acad. Sci. U.S.A.* **91**, 6735–6742 (1994).
53. E. D. Swanner, A. M. Mloszewska, O. A. Cirpka, R. Schoenberg, K. O. Konhauser, A. Kappler, Modulation of oxygen production in Archaean oceans by episodes of Fe(II) toxicity. *Nat. Geosci.* **8**, 126–130 (2015).
54. A. M. Mloszewska, D. B. Cole, N. J. Planavsky, A. Kappler, D. S. Whitford, G. W. Owttrim, K. O. Konhauser, UV radiation limited the expansion of cyanobacteria in early marine photic environments. *Nat. Commun.* **9**, 3088 (2018).
55. G. J. Dick, S. L. Grim, J. M. Klatt, Controls on O_2 production in cyanobacterial mats and implications for Earth's oxygenation. *Annu. Rev. Earth Planet. Sci.* **46**, 123–147 (2018).
56. A. H. Knoll, R. K. Bambach, Directionality in the history of life: Diffusion from the left wall or repeated scaling of the right? *Paleobiology* **26**, 1–14 (2000).
57. J. Zhang, P. D. Quay, D. O. Wilbur, Carbon isotope fractionation during gas-water exchange and dissolution of CO_2. *Geochim. Cosmochim. Acta* **59**, 107–114 (1995).
58. C. S. Romanek, E. L. Grossman, J. W. Morse, Carbon isotopic fractionation in synthetic aragonite and calcite: Effects of temperature and precipitation rate. *Geochim. Cosmochim. Acta* **56**, 419–430 (1992).
59. T. M. Lenton, S. J. Daines, B. J. W. Mills, COPSE reloaded: An improved model of biogeochemical cycling over Phanerozoic time. *Earth Sci. Rev.* **178**, 1–28 (2018).
60. A. P. Gumsley, K. R. Chamberlain, W. Bleeker, U. Söderlund, M. O. de Kock, E. R. Larsson, A. Bekker, Timing and tempo of the Great Oxidation Event. *Proc. Natl. Acad. Sci.* **114**, 1811–1816 (2017).
61. C. J. Bjerrum, D. E. Canfield, Ocean productivity before about 1.9 Gyr ago limited by phosphorus adsorption onto iron oxides. *Nature* **417**, 159–162 (2002).
62. K. Fennel, M. Follows, P. G. Falkowski, The co-evolution of the nitrogen, carbon and oxygen cycles in the Proterozoic ocean. *Am. J. Sci.* **305**, 526–545 (2005).
63. A. D. Anbar, A. H. Knoll, Proterozoic ocean chemistry and evolution: A Bioinorganic bridge? *Science* **297**, 1137–1142 (2002).

64. D. T. Johnston, F. Wolfe-Simon, A. Pearson, A. H. Knoll, Anoxygenic photosynthesis modulated Proterozoic oxygen and sustained Earth's middle age. *Proc. Natl. Acad. Sci.* **106**, 16925–16929 (2009).
65. N. J. Butterfield, Oxygen, animals and oceanic ventilation: An alternative view. *Geobiology* **7**, 1–7 (2009).
66. P. Sánchez-Baracaldo, A. Ridgwell, J. A. Raven, A Neoproterozoic transition in the marine nitrogen cycle. *Curr. Biol.* **24**, 652–657 (2014).
67. T. L. Hamilton, D. A. Bryant, J. L. Macalady, The role of biology in planetary evolution: Cyanobacterial primary production in low-oxygen Proterozoic oceans. *Environ. Microbiol.* **18**, 325–340 (2016).
68. J. F. Allen, B. Thake, W. F. Martin, Nitrogenase inhibition limited oxygenation of Earth's proterozoic atmosphere. *Trends Plant Sci.* **24**, 1022–1031 (2019).
69. R. E. Summons, J. M. Hayes, Principles of molecular and isotopic biogeochemistry, in *The Proterozoic Biosphere, a Multidisciplinary Study*, J. W. Schopf, C. Klein, Eds. (Cambridge Univ. Press, 1992), pp. 83–94.
70. S. E. Stevens Jr., C. O. P. Patterson, J. Myers, The production of hydrogen peroxide by blue-green algae: A survey[1]. *J. Phycol.* **9**, 427–430 (1973).
71. R. E. Zeebe, D. Wolf-Gladrow, *CO_2 in Seawater: Equilibrium, Kinetics, Isotopes* (Oceanography Series, Elsevier, ed. 1, 2001), vol. 65.
72. C. G. Trick, S. W. Wilhelm, Physiological changes in the coastal marine cyanobacterium *Synechococcus sp.* PCC 7002 exposed to low ferric ion levels. *Mar. Chem.* **50**, 207–217 (1995).
73. R. D. Guy, M. L. Fogel, J. A. Berry, Photosynthetic fractionation of the stable isotopes of oxygen and carbon. *Plant Physiol.* **101**, 37–47 (1993).
74. D. B. McNevin, M. R. Badger, S. M. Whitney, S. von Caemmerer, G. G. B. Tcherkez, G. D. Farquhar, Differences in carbon isotope discrimination of three variants of D-ribulose-1,5-bisphosphate carboxylase/oxygenase reflect differences in their catalytic mechanisms. *J. Biol. Chem.* **282**, 36068–36076 (2007).
75. R. L. Clark, J. C. Cameron, T. W. Root, B. F. Pfleger, Insights into the industrial growth of cyanobacteria from a model of the carbon-concentrating mechanism. *AIChE J.* **60**, 1269–1277 (2014).
76. P. J. Thomas, A. J. Boller, S. Satagopan, F. R. Tabita, C. M. Cavanaugh, K. M. Scott, Isotope discrimination by form IC RubisCO from *Ralstonia eutropha* and *Rhodobacter sphaeroides*,

metabolically versatile members of *'Proteobacteria'* from aquatic and soil habitats. *Environ. Microbiol.* **21**, 72–80 (2019).

77. E. B. Wilkes, A. Pearson, A general model for carbon isotopes in red-lineage phytoplankton: Interplay between unidirectional processes and fractionation by RubisCO. *Geochim. Cosmochim. Acta* **265**, 163–181 (2019).
78. R. E. Zeebe, On the molecular diffusion coefficients of dissolved CO_2, HCO_3^-, and CO_3^{2-} and their dependence on isotopic mass. *Geochim. Cosmochim. Acta* **75**, 2483–2498 (2011).
79. M. H. O'Leary, Measurement of the isotope fractionation associated with diffusion of carbon dioxide in aqueous solution. *J. Phys. Chem.* **88**, 823–825 (1984).